applied sciences

MDPI

Article

Research on Flame Temperature Measurement Technique Combining Spectral Analysis and Two-Color Pyrometry

Pan Pei, Xiaojian Hao *, Shenxiang Feng, Tong Wei and Chenyang Xu

State key Laboratory of Extreme Environment Optoelectronic Dynamic Testing Technology and Instrument, North University of China, Taiyuan 030051, China; b20210622@st.nuc.edu.cn (P.P.); b20240602@st.nuc.edu.cn (S.F.); sz202206038@st.nuc.edu.cn (T.W.); s202206123@st.nuc.edu.cn (C.X.)

* Correspondence: haoxiaojian@nuc.edu.cn

Abstract: This work presents a method for measuring flame temperatures through an imaging technique that combines spectral analysis with two-color pyrometry. Initially, we employed Laser-Induced Breakdown Spectroscopy (LIBS) to analyze the radiation spectrum of nitrocellulose, selecting 694 nm and 768 nm as the two spectral lines for temperature measurement. Subsequently, we constructed a temperature measurement system utilizing two sCMOS cameras and conducted calibration within the range of 600 to 1000 °C, achieving a maximum temperature measurement uncertainty of 3.43%. Finally, we successfully performed two-dimensional temperature field detection and imaging of nitrocellulose flames of varying qualities, achieving a flame image resolution of 2048 (H) × 2048 (V). In comparison to traditional two-color infrared thermometers and Tunable Diode Laser Absorption Spectroscopy (TDLAS) technology, the maximum relative temperature measurement error was 2.1%. This work provides technical insights into the development of high-resolution, low-cost flame temperature imaging technology applicable across a wide range of fields.

Keywords: sCMOS sensors; optical imaging; temperature measurement; spectral analysis; two-color pyrometry



Academic Editor: Zhengjun Liu

Received: 18 April 2025
Revised: 21 May 2025
Accepted: 22 May 2025
Published: 23 May 2025

Citation: Pei, P.; Hao, X.; Feng, S.; Wei, T.; Xu, C. Research on Flame Temperature Measurement Technique Combining Spectral Analysis and Two-Color Pyrometry. *Appl. Sci.* **2025**, *15*, 5864. https://doi.org/10.3390/app15115864

Copyright: © 2025 by the authors. Licensee MDPI, Basel, Switzerland. This article is an open access article distributed under the terms and conditions of the Creative Commons Attribution (CC BY) license (https://creativecommons.org/licenses/by/4.0/).

1. Introduction

Temperature, one of the seven fundamental physical quantities in the International System of Units, holds significant importance for both industrial production [1–3] and the frontiers of scientific research [4–6]. Current temperature measurement technologies are primarily categorized into two types: contact measurement and non-contact measurement. Contact temperature measurement technologies, such as thermocouples [7,8], are generally well established for typical applications. However, the intrusion of sensors into the temperature field can disrupt the surrounding flow field, and their relatively slow response times can adversely affect measurement accuracy. In contrast, non-contact temperature measurement technologies, particularly those based on radiation measurement [9–11], do not disturb the measured temperature field. These technologies are characterized by rapid response times and a wide measurement range, and they are currently experiencing rapid development.

Experts and scholars have studied the measurement methods of flame temperature. Flame temperature measurement methods include planar laser-induced fluorescence (PLIF) [12], coherent anti-Stokes Raman scattering spectroscopy (CARS) [13], and Rayleigh scattering imaging [14]; however, these methods require expensive equipment and complex optical systems.

Infrared thermography [15,16] can determine the temperature of the object to be measured by measuring the infrared radiation of the object itself. Infrared temperature measurement does not affect the temperature field, has high sensitivity and responsivity, is convenient to realize the dynamic observation of flames, has a wide range of temperature measurements, and can be used for night vision operations; however, the infrared temperature measurement method mainly depends on the emissivity, but the actual emissivity value is unknown in many cases. The working bands of the infrared thermal imaging cameras are divided into three bands: short wave ($1-2.5$ μm), medium wave ($2-5$ μm), and long wave ($8-14$ μm). The wavelength bands of $2-5$ μm and $8-14$ μm are the two atmospheric windows commonly used by infrared thermal imaging cameras. In this range, the atmospheric transmittance is large, and the attenuation of infrared radiation is small, which is commonly used to measure temperature.

Many scholars have combined digital image processing technology with the well-developed principle of single-wavelength radiation thermometry of visible light [17,18] to measure the two-dimensional temperature field of the flame through the temperature calibration of the camera; however, the emissivity of the measured object still needs to be obtained. Multispectral temperature measurement technology [19,20] requires the selection of an appropriate emissivity model. This model establishes a hypothetical relationship between spectral emissivity and temperature or wavelength to simplify the unknowns. It combines data from multiple spectral channels to establish a temperature measurement model through the optimization of multi-order equations. However, the relationship assumptions of different analytes vary greatly, leading to low universality of the hypothetical relationship.

Two-color pyrometry technology has been widely used in temperature measurement, compared with the above-mentioned thermometric method, which needs to consider how to accurately measure emissivity. The two-color pyrometry method can usually ignore the influence of emissivity and optical noise in the process of acquiring images on the temperature measurement accuracy when the selected working band is approximate, and the accuracy is greatly improved.

Campbell N R [21] was the first to propose this idea and used the two-color pyrometry developed by it to measure the temperature. Zhou H C [22,23] calculated the three-dimensional distribution field of flame temperature and emissivity using two-color pyrometry thermometry. Yan W et al. [24] calculated the temperature and emissivity curves of a solid waste incinerator using spectral data and the two-color pyrometry method. The operation of this method is simple, but it can only obtain the temperature information of the flame, not the spatial information of the flame.

With the development of optical technology, two-color pyrometry technology has evolved from spot temperature measurement [25,26] to being combined with CMOS and CCD imaging technologies [27,28] to achieve higher spatial resolution and higher precision temperature measurement.

CHENG Y F [29] developed an improved two-color pyrometry high-temperature measuring instrument for suspended tungsten powder, solving the problem that the absolute RGB value of each pixel cannot be calculated. A two-color ratio analysis was performed to calculate the temperature of each pixel, and the average G/R ratio of each pixel was calculated based on the surrounding 3×3 matrices. Corral-Gómez [30] used a high-speed CMOS camera to measure the formation of combustion soot from engines based on temperature measurement technology, and methodological studies on the influence of the dynamic range and wavelength used in the detector. Sawada S [31] used two-color pyrometry thermometry to study the flame structure of pulverized coal combustion and the time series of flame temperature and particle temperature. The results showed that the

increase in oxygen concentration raised the combustion temperature and flame diameter of volatiles and extended the special duration of volatile combustion. HU K [32] obtained the two-dimensional temperature field of the Mg/CO_2 combustion flame by constructing a Mg/CO_2 combustion device and a two-color pyrometry temperature measurement system based on a color charge-coupled device (CCD). The experimental results verified the accuracy of temperature measurement of high-temperature objects based on the color CCD radiation imaging method.

Although the existing two-color thermometry methods are able to solve the problem of flame spatial and spectral information, there is almost no elaboration on the selection of temperature measurement spectra, and the range of temperature measurement spectra. The range of temperature spectra, as well as the selection of wavelength intervals of the dual-band, affects the accuracy of temperature measurement to a certain extent.

The primary objective of this study is to detect the flame temperature field using spectral analysis in conjunction with two-color thermometry. The combustion radiation spectrum was obtained through Laser-Induced Breakdown Spectroscopy (LIBS) technology, and the optimal spectral line for temperature measurement was selected based on the principles of two-color thermometry. This approach effectively eliminates the influence of the emissivity of the measurement target. The temperature measurement system was calibrated at temperatures ranging from 600 to 1000 °C using a commercial standard blackbody source. The detection of the nitrocellulose flame temperature was achieved by analyzing the images acquired from two wavebands. Compared to traditional colorimetric temperature measuring instruments, this method provides a more accurate two-dimensional temperature image of the flame, with a measurement error of within 3%.

2. Materials and Methods

2.1. Principle of Two-Color Pyrometry

The most basic principle of the two-color thermometry method is Planck's law of radiation [33], where the spectral radiance emitted by an object is related to wavelength and temperature as in Equation (1):

$$M(\lambda, T) = \frac{1}{\pi}\varepsilon(\lambda)\frac{C_1}{\lambda^5}\exp(1 - \frac{C_2}{\lambda T}), \tag{1}$$

$M(\lambda, T)$ is the monochromatic radiant exitance at a given wavelength λ and temperature T, $\varepsilon(\lambda)$ is the monochromatic emissivity for a given wavelength, T is absolute temperature, K; the first radiation constant $C_1 = 2\pi hc^2$, the second radiation constant $C_2 = hc/k$, h is the Planck constant, k is the Boltzmann constant, c is the speed of light, $C_1 = 3.7415 \times 10^8 W \cdot \mu m^4 \cdot m^{-2}$, $C_2 = 1.4388 \times 10^4 \mu m \cdot K$.

When the condition $\lambda T \leq 2000\ \mu m \cdot K$ is satisfied, $M_b(\lambda, T)$ is a monochromatic blackbody radiant exitance, Planck's law can be replaced by Wien's law:

$$\begin{array}{l} M(\lambda, T) \approx \frac{1}{\pi}\varepsilon(\lambda)\frac{C_1}{\lambda^5}\exp(-\frac{C_2}{\lambda T}) = \varepsilon(\lambda)M_b(\lambda, T) \\ M_b(\lambda, T) = \frac{1}{\pi}\frac{C_1}{\lambda^5}\exp(-\frac{C_2}{\lambda T}) \end{array}, \tag{2}$$

If the monochromatic radiant exitance $M(\lambda_1, T), M(\lambda_2, T)$ of the two spectral lines λ_1, λ_2 can be obtained, their division provides the following two-color ratio Equation (3):

$$\frac{M(\lambda_1, T)}{M(\lambda_2, T)} = \left(\frac{\varepsilon_{\lambda_1}}{\varepsilon_{\lambda_2}}\right)\frac{{\lambda_2}^5}{{\lambda_1}^5} \times \exp\left[-\frac{C_2}{T}\left(\frac{1}{\lambda_1} - \frac{1}{\lambda_2}\right)\right], \tag{3}$$

Finally, we obtain the two-color thermometry Equation (4):

$$T = -C_2\left(\frac{1}{\lambda_1} - \frac{1}{\lambda_2}\right) / \ln\left(\frac{M_b(\lambda_1, T)}{M_b(\lambda_2, T)} \frac{\varepsilon_{\lambda 2}}{\varepsilon_{\lambda_1}} \frac{\lambda_1^5}{\lambda_2^5}\right), \tag{4}$$

The selected wavelength range for calculating temperature was based on the following principles [34]: First, spectral lines that exhibit significant variations in intensity within the flame should be avoided. Second, it is essential to ensure high signal-to-noise ratios for the spectral measurement data by excluding the beginning and end of the spectral measurement range. If the spectral emissivity varies with wavelength and the relationship between them is unknown, the two-color method is not applicable for temperature measurements. Therefore, when employing the two-color temperature measurement technique, it is crucial to ensure that the flame adheres to the gray body property, which means that the emissivities are approximately equal within the chosen spectral range.

2.2. Spectral Analysis of Energy-Containing Materials

2.2.1. Spectral Analysis Using Laser-Induced Breakdown Spectroscopy

In this paper, we utilized the Chem Reveal benchtop laser-induced breakdown spectrometer (TSI, Shoreview, MN, USA), which is equipped with an Nd:YAG laser from Quantel, France, operating at a wavelength of 1064 nm and capable of delivering energy ranging from 20 to 200 mJ. The optical system includes a seven-channel wide-range spectrometer from Avantes, Netherlands, with a spectral range of 190 nm to 950 nm and a spectral resolution of 0.1 nm. The appearance and schematic diagram of the instrument are presented in Figure 1, which primarily consists of a laser, a spectrometer, an optical system, a three-dimensional carrier stage, and a computer. To obtain spectral information about the energy-containing materials, we employed the Laser-Induced Breakdown Spectroscopy (LIBS) technique [35,36] to analyze the elements present in nitrocellulose and their characteristic spectral lines, in conjunction with the NIST spectral database. The two most suitable bands were selected as the detection wavelengths for two-color temperature measurements.

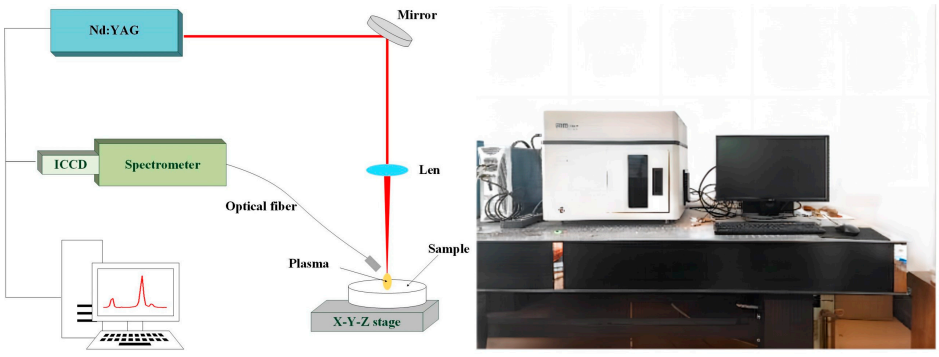


Figure 1. Chem Reveal laser-induced breakdown spectrometer and principle. (**a**) LIBS schematic; (**b**) LIBS Device Diagram.

LIBS (Laser-Induced Breakdown Spectroscopy) technology employs a high-energy laser to interact with the surface of the object being measured, generating plasma that emits spectral information. This spectral signal is transmitted to a spectrometer through an optical system, and the collected spectral lines are processed and analyzed using computer software.

Due to the substantial laser output energy of the LIBS (Laser-Induced Breakdown Spectroscopy) system, which can reach up to 200 mJ, the nitrocellulose sample was burned

on a 310 stainless steel substrate to protect the spectrometer's detection lens from contamination. The nitrocellulose combustion product was then placed on the stage for analysis to obtain the spectral data of the nitrocellulose sample. Laser measurement did not trigger the combustion of nitrocellulose.

Figure 2 illustrates the appearance of nitrocellulose before and after combustion. The LIBS (Laser-Induced Breakdown Spectroscopy) emission spectra of nitrocellulose at energy levels of 80, 90, 100, 110, and 120 mJ were recorded by directing a high-energy laser at the burned nitrocellulose samples, as depicted in Figure 3. The overall consistency of the spectra was satisfactory. According to data from the National Institute of Standards and Technology (NIST) spectral database, potassium (K) exhibits a notably strong excitation spectrum in the visible range, with no nearby interference bands. This suggests that potassium may be an intrinsic element of nitrocellulose, and the characteristic wavelength associated with this peak can be utilized for subsequent temperature measurements.



(**a**) (**b**)

Figure 2. Picture of nitrocellulose samples and combustion products. (**a**) Nitrocellulose samples; (**b**) Nitrocellulose combustion products diagram.

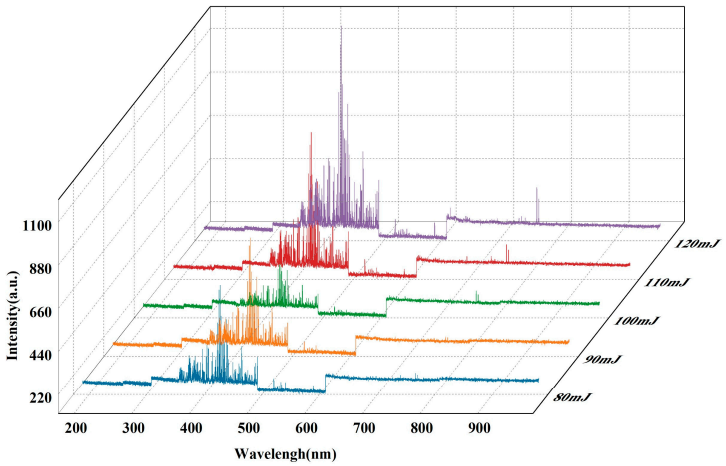


Figure 3. Spectrogram of nitrocellulose by LIBS.

Figure 4 illustrates the average energy spectrum of nitrocellulose residues. The potassium (K) element exhibits prominent spectral line peaks at 404.4 nm, 766.3 nm, and 769.8 nm. Notably, the spectral lines near 404.4 nm are more convoluted due to interference from other lines, while the peaks at 766.3 nm and 769.8 nm are relatively distinct and unaffected by surrounding spectral lines.

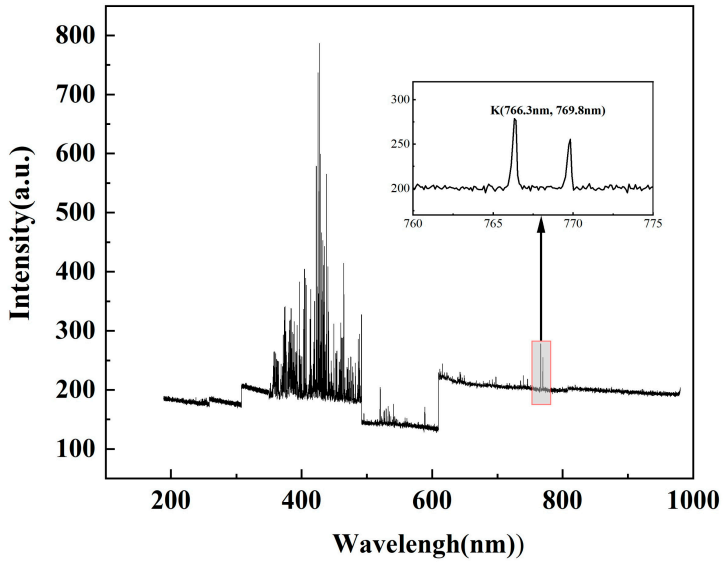


Figure 4. Average spectrum of nitrocellulose residues.

2.2.2. Band Selection for Two-Color Temperature Measurements

Potassium (K) is commonly found in biomass fuels [37] and various energy-containing materials [38]. Consequently, characteristic spectra of the element K can be emitted during the combustion of these materials or the detonation of munitions.

Referring to the NIST (National Institute of Standards and Technology) spectral database [39], we can identify the wavelengths corresponding to the prominent spectral peaks of K (404.4 nm, 691.1 nm, 693.8 nm, 766.3 nm, and 769.8 nm) in the visible range. Notably, the spectral lines at 691.1 nm and 693.8 nm of potassium are consistently observed in a variety of compounds found in different energy-containing materials [40].

The wavelength interval in the two-color method is a critical parameter for calculating temperature. To ensure the accuracy of the calculated temperature, the wavelength interval should be at least 30 nm [41]. Consequently, we selected two spectral lines, 694 nm and 768 nm, for temperature testing based on our previous research [42–44].

The intervals between the wavelengths were set to 10 nm, 20 nm, 30 nm, 40 nm, 50 nm, and 60 nm to investigate the effect of wavelength intervals on the accuracy of temperature measurements at 800 °C, as shown in Table 1.

Table 1. Error results of blackbody temperature measurement for 800 °C.

Wavelength Interval (nm)	10	20	30	40	50	60
Error (%)	3.80	2.41	1.52	0.79	0.80	0.80

When the wavelength interval is 10 nm, the temperature distribution fluctuates significantly with the wavelength, resulting in a temperature measurement error of 3.8%. For wavelength intervals greater than 30 nm, the temperature measurement error decreases as the wavelength interval increases, falling below 1% at 40 nm and 60 nm, both measuring 0.8%. This indicates that there is no significant difference in temperature measurements at intervals greater than 40 nm. Therefore, to ensure the accuracy of the calculations, the wavelength interval should be at least 30 nm or greater.

2.3. Temperature Calibration Experiment

The temperature field detection imaging in this study was mainly realized using visible light cameras, specifically two Tucsen Photonics DHYANA 400BSI V2 sCMOS cameras [45] (Tucsen, Fuzhou, China), with image resolutions of 2048 × 2048 and an image frame rate

of 40 Hz. For spectral analysis based on energy-containing materials above, we choose $\lambda_1 = 694 \pm 10$ nm and $\lambda_2 = 768 \pm 10$ nm, two kinds of narrow-band filters installed in front of the camera lens for temperature field narrow-band filter detection. The temperature field detection imaging module is shown in Figure 5.



(**a**) (**b**)

Figure 5. Two-color thermometry cameras. (**a**) Physical view of the sCMOS cameras; (**b**) Filter and mounting bracket.

Compared with other papers [22–38], the resolution of the temperature measurement image in this paper has been greatly improved, reaching 2048×2048 image pixels with a spatial frequency of 76.92 Ip/mm. This method has the advantage of achieving higher-resolution two-dimensional imaging of flames.

Before acquiring images of the temperature field using two high-precision scientific cameras, the DHYANA 400BSI V2, it is essential to calibrate the cameras, as illustrated in Figure 6. The optical path employs a beamsplitter with a discrete beam splitter to facilitate simultaneous image acquisition by both cameras—one equipped with a 694 nm filter and the other with a 768 nm filter. Both cameras are configured with identical parameters: an exposure time of 100 microseconds, an aperture of f/1.4, and each camera utilizes a 2/3-inch lens with a focal length of 50 mm. The two cameras capture the same target temperature information through the beamsplitter, and a synchronous trigger device ensures that both cameras collect temperature data simultaneously, which is then transmitted to a computer for processing.

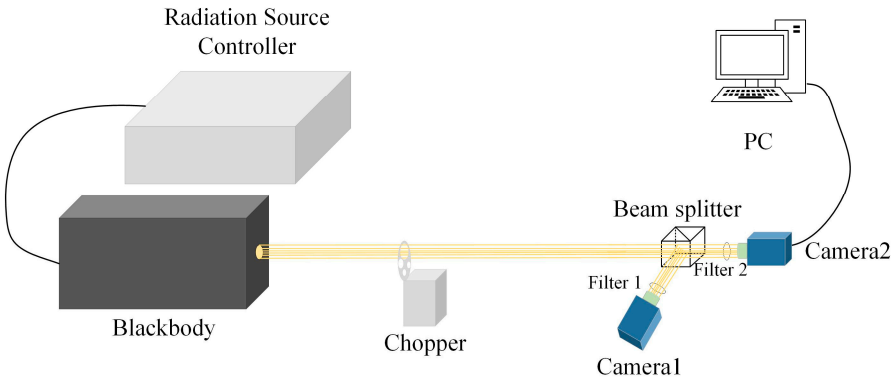


Figure 6. Schematic diagram of the calibration experiment.

In this study, we utilized the medium-temperature blackbody furnace SR20-32 from CI, Israel, as the standard temperature radiation source. This furnace features a blackbody cavity with an inner diameter of 25.4 mm, a length of 100 mm, and a spectral emissivity of approximately 0.99. We conducted a temperature calibration of the camera for the range of 600 to 1000 °C. The calibration experiment was arranged as illustrated in Figure 6, with the imaging system positioned 0.5 m away from the opening of the blackbody furnace cavity. The lens focus was adjusted to ensure a clear and stable image. Two sCMOS cameras were employed to capture images at intervals of 25 °C, starting from 600 °C, resulting in a total

of 17 acquisitions. Upon completion of the image acquisition, the grayscale images at each temperature were processed in batches to extract the relevant luminescence data from the blackbody cavity. Subsequently, we averaged the grayscale values within the designated region and fitted the relationship between spectral irradiance and the average grayscale value at various temperatures of the blackbody.

When utilizing a blackbody furnace for calibration, the blackbody is set to different temperature values to ultimately establish a functional relationship between the gray value and the radiant emittance:

$$G = kM(\lambda, T) + b, \tag{5}$$

As shown in Figure 7, the monochromatic image of the blackbody cavity in the mid-temperature segment calibration at 600 °C~1000 °C at 694 nm reveals that the imaging gray value G correlates with the blackbody spectral radiation outgoing degree of the curve, as shown in Figure 8 An approximately linear relationship between the changes in the fitting relationship is expressed in Equation (6):

$$G_1 = 0.4891M_1 + 6.3508, \tag{6}$$

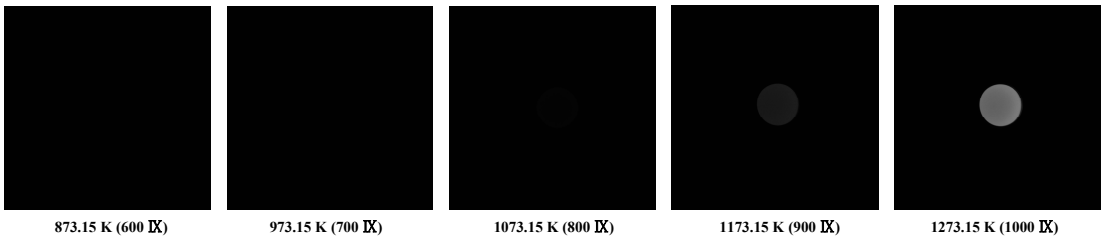


Figure 7. Monochrome image of blackbody cavity at 694 nm from 600 °C to 1000 °C.

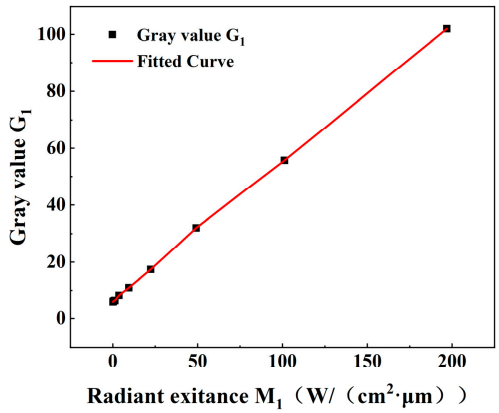


Figure 8. The relationship between G_1 and M_1.

Figure 9 shows that the blackbody cavity in the mid-temperature section of the calibration at 600–1000 °C under the 768 nm monochrome image, the imaging gray value G, and the blackbody spectral radiation outgoing degree of the curve, as shown in Figure 10, illustrate an approximately linear relationship between the change in the fitting relationship expressed as Equation (7):

$$G_2 = 0.3684M_2 + 10.738, \tag{7}$$

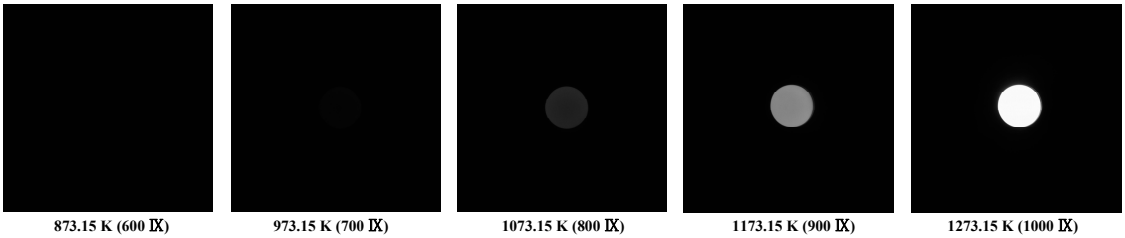


Figure 9. Monochrome image of a blackbody cavity at 768 nm from 600 °C to 1000 °C.

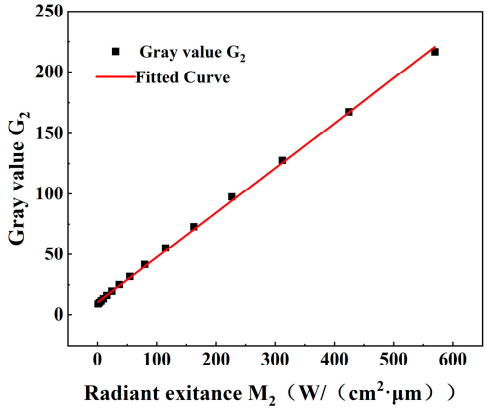


Figure 10. The relationship between G_2 and M_2.

Substituting Equation (5) into Equation (4), according to the gray body hypothesis, for two spectral lines with small intervals, the emissivity ε_{λ_1}, ε_{λ_2} ratio is approximated as 1; thus, the emissivity can be eliminated. We can finalize the temperature T expression for two-color thermometry:

$$T = C_2\left(\frac{1}{\lambda_2} - \frac{1}{\lambda_1}\right)/\left(\ln\frac{G_1 - b_1}{G_2 - b_2} + \ln\frac{k_2}{k_1} + 5\ln\frac{\lambda_1}{\lambda_2}\right), \quad (8)$$

where λ_1, λ_2, nm, $C_2 = 1.4388 \times 10^4 \mu m \cdot K$.

3. Results

3.1. Accuracy and Uncertainty Analysis

The two-color pyrometry temperature measurement method is used to measure nine standard temperatures in the range of 600–1000 °C in the blackbody furnace, and the average value of the nine measured temperatures is taken as the measurement result. In Table 2, the temperature measurement error = |two-color temperature − blackbody temperature| / blackbody temperature × 100%. The method, in the temperature range of 600–1000 °C, shows that the measurement error is basically within 2.5%, and the range of error is 0.61–2.31%. Figure 11 gives the temperature curves and measurement errors for nine temperature points, with the measurement errors in the high-temperature section all exceeding 1.2%. This may be due to the fact that the camera, which has an 8-bit pixel depth, increases the nonlinearity of the camera's response as the temperature rises. Additionally, with the emergence of image noise, the temperature measurement error gradually increases.

Table 2. Error analysis of two-color pyrometry.

Sampling Point	G_1	G_2	Blackbody Temperature/°C	Two-Color Pyrometry Temperature/°C	Temperature Measurement Error/%
1	6	9.1	600	605.63	0.94
2	6.29	10.5	650	653.96	0.61
3	6.7	11.89	700	706.26	0.89
4	8.26	16.68	750	764.38	1.92
5	11	24	800	812.61	1.58
6	17.37	39.6	850	866.47	1.94
7	32	72.89	900	920.76	2.31
8	55.77	122.5	950	970.68	2.18
9	102	216.51	1000	1012.63	1.26

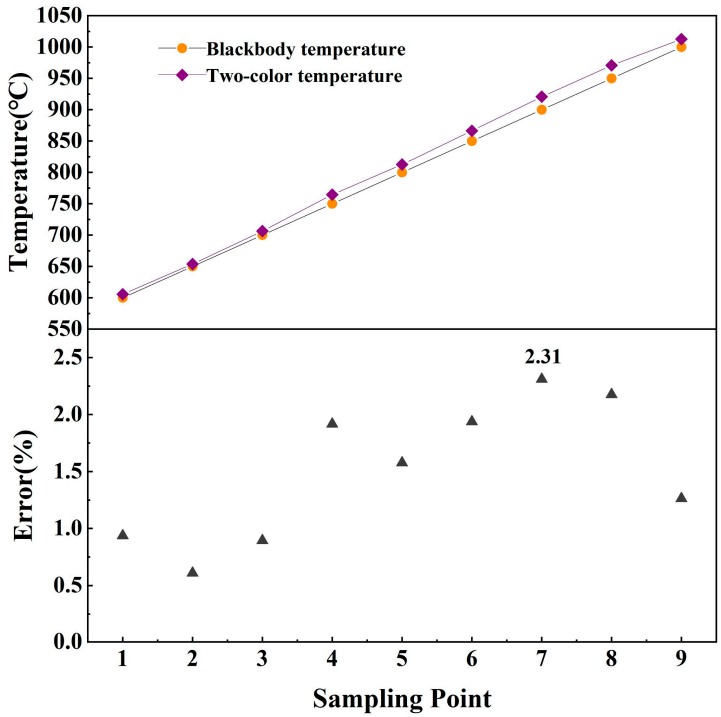


Figure 11. Temperature measurement error curve.

A logarithmic differentiation method has been used to evaluate temperature uncertainty, on the basis of Equation (8). The main sources of uncertainty lie in the gray body hypothesis, in the interference filters, and in the conversion procedure from spectral radiance to gray scale levels [46]. Table 3 shows the values of each parameter at 600–1000 °C.

Table 3. Constant parameter values used for uncertainty computations.

	600 °C	650 °C	700 °C	750 °C	800 °C	850 °C	900 °C	950 °C	1000 °C
N_{G_1,G_2,b_1,b_2}	0.177	0.058	0.130	0.351	0.322	0.357	0.413	0.422	0.465
K_{λ_1,λ_2}	0.75	0.75	0.75	0.75	0.75	0.75	0.75	0.75	0.75
F	1.083	1.026	1.060	1.172	1.157	1.175	1.205	1.210	1.234
$\Delta N_{G_1,G_2,b_1,b_2}$	0.00247	0.00125	0.00133	0.00164	0.00060	0.00201	0.01128	0.00216	0.00478

The $\frac{G_1-b_1}{G_2-b_2}$ is replaced by N_{G_1,G_2,b_1,b_2}, where $K_{\lambda_1,\lambda_2} = \frac{k_2}{k_1}$, then we named F:

$$F = \ln\frac{G_1-b_1}{G_2-b_2} + \ln\frac{k_2}{k_1} + 5\ln\frac{\lambda_1}{\lambda_2} = \ln(N_{G_1,G_2,b_1,b_2}K_{\lambda_1,\lambda_2}\frac{{\lambda_1}^5}{{\lambda_2}^5}), \tag{9}$$

3.1.1. Uncertainty of Gray Body Assumption

The gray body assumption postulates that the ratio of the values of the emissivity at small intervals of wavelengths λ_1 and λ_2, with small intervals, is equal to 1.

$$U_{\varepsilon_R} = \Delta\varepsilon_R\left|\frac{1}{F\varepsilon_R}\right|, \tag{10}$$

The uncertainties are then computed as a function of the different emissivity ratios ε_R, and an uncertainty of $\Delta\varepsilon_R = 1\%$ on the emissivity ratio is chosen.

3.1.2. Uncertainty of Interference Filters

The interference filter used in two-color thermometry is a narrowband filter with a bandwidth of 10 nm, the uncertainty of each wavelength is half bandwidth, $\Delta\lambda_1 = \Delta\lambda_2 = 5$ nm.

$$U_{\lambda_1,\lambda_2} = \Delta\lambda_1\left|-\frac{5}{F\lambda_1} + \frac{1}{\lambda_1-\lambda_2} - \frac{1}{\lambda_1}\right| + \Delta\lambda_2\left|\frac{5}{F\lambda_2} - \frac{1}{\lambda_1-\lambda_2} + \frac{1}{\lambda_2}\right|, \tag{11}$$

3.1.3. Uncertainty of Conversion from Radiance to Gray Scale Level

This conversion process integrates the complete process of converting spectral radiation to gray levels. It takes into account the whole optical path, the camera sensors, and the associated uncertainties. The relative change in the measured temperature due to the change in the sensitivity coefficients K_{λ_1,λ_2} is:

$$U_{K_{\lambda_1,\lambda_2}} = \Delta K_{\lambda_1,\lambda_2}\left|\frac{1}{FK_{\lambda_1,\lambda_2}}\right|, \tag{12}$$

From the calibration fitting curve, it can be seen that $\Delta K_{\lambda_1,\lambda_2}$ takes the maximum value of 0.01. The uncertainty caused by the noise and nonlinearity of the camera is related to the gray value G and the offset b, so we can obtain:

$$U_{N_{G_1,G_2,b_1,b_2}} = \Delta N_{G_1,G_2,b_1,b_2}\left|\frac{1}{FN_{G_1,G_2,b_1,b_2}}\right|, \tag{13}$$

$\Delta N_{G_1,G_2,b_1,b_2}$ is the maximum offset at each temperature.

Synthetic Standard Uncertainty U is:

$$U = \sqrt{{U_{\varepsilon_R}}^2 + {U_{\lambda_1,\lambda_2}}^2 + {U_{K_{\lambda_1,\lambda_2}}}^2 + {U_{N_{G_1,G_2,b_1,b_2}}}^2}, \tag{14}$$

Based on the above formula, we have obtained uncertain parameters at different temperatures, as shown in Table 4:

Table 4. Summary of uncertain parameters.

	600 °C	650 °C	700 °C	750 °C	800 °C	850 °C	900 °C	950 °C	1000 °C
U_{ε_R}	0.92%	0.97%	0.94%	0.85%	0.86%	0.85%	0.83%	0.83%	0.81%
U_{λ_1,λ_2}	2.13%	2.17%	2.15%	2.09%	2.09%	2.08%	2.07%	2.07%	2.06%
$U_{K_{\lambda_1,\lambda_2}}$	1.23%	1.30%	1.26%	1.14%	1.15%	1.13%	1.11%	1.10%	1.08%
$U_{N_{G_1,G_2,b_1,b_2}}$	1.29%	2.11%	0.97%	0.40%	0.16%	0.48%	2.27%	0.42%	0.83%
U	2.93%	3.43%	2.83%	2.56%	2.55%	2.57%	3.37%	2.52%	2.60%

Therefore, we can conclude that in the range of 600 °C~1000 °C, the standard uncertainty distribution range of the two-color thermometry system is 2.52%~3.43%.

Consequently, the maximum temperature measurement error of our two-color pyrometry temperature measurement system is 2.31%, and the maximum temperature measurement uncertainty is 3.43%. In the future, the wavelength interval selection and the black body furnace performance can be further optimized to reduce the uncertainty of temperature measurement.

3.2. Nitrocellulose Experiments and Results

The 0.3 g nitrocellulose sample was placed on the shelf at a distance of 0.5 m from the sCMOS camera. The nitrocellulose was ignited on-site, and the camera collected a complete flame image. The nitrocellulose burning time was about 2 s, and the collected flame image was brought into the two-color temperature measurement formula. Finally, the temperature image of the nitrocellulose burning flame was obtained, and the temperature images of some typical moments of the flame were recorded in Figure 12. There are three main stages of combustion:

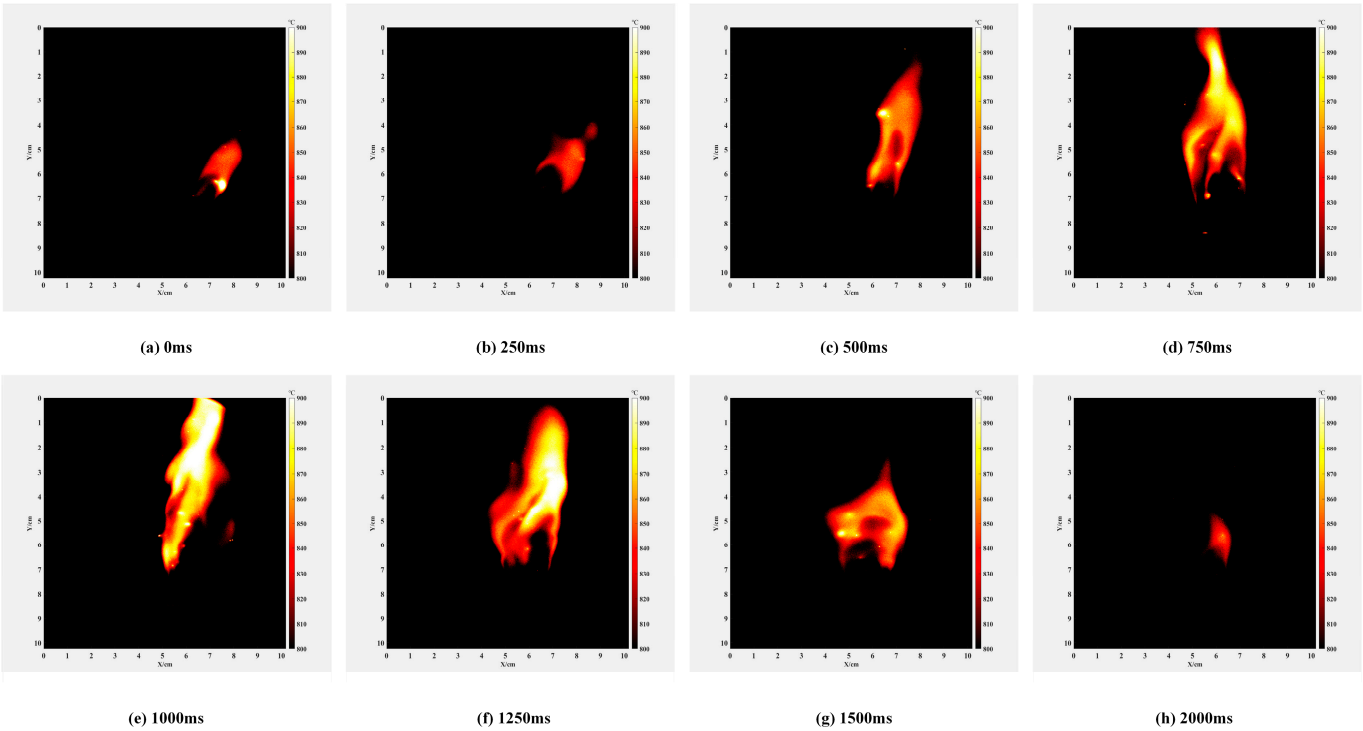


Figure 12. Temperature images at different moments of 0.3 g nitrocellulose flame.

(1) Figure 12a–d of the combustion diffusion stage: the flame gradually spreads and becomes larger from 1.895 cm wide and 4.3 cm high in the initial Figure 12a, with

the flame temperature gradually increasing. The flame in Figure 12d also increases significantly, reaching 3.52 cm wide and 7.67 cm high;

(2) Figure 12e,f in the full combustion stage: with the expansion of the contact area between the nitrocellulose flame and oxygen, some alkali metals inside the nitrocellulose are violently burned, the flame has some obvious bright spots, and the temperature is also significantly increased, the width of the flame is more than 3.6 cm, the height is more than 7.7 cm, and the maximum temperature of the flame reaches 993.7 °C at the time of 1000 ms in Figure 12e;

(3) Figure 12g,h of the combustion dissipation stage: with the passage of time, the composition of the energetic material gradually decreases, the temperature of the flame also decreases gradually, and the flame becomes smaller and smaller until it is extinguished. The size of the flame is 1.91 cm wide and 4.9 cm high at 2000 ms.

In order to more intuitively see the temperature change process of the nitrocellulose flame, the centerline temperature change curve of the nitrocellulose flame at 1000 ms was plotted, as shown in Figure 13. The temperature change in the centerline shows a gradual increase first, reaching a maximum temperature of 921.8 °C, and then the temperature began to gradually decline. There is a small increase in the middle, but it soon began to decline continuously.

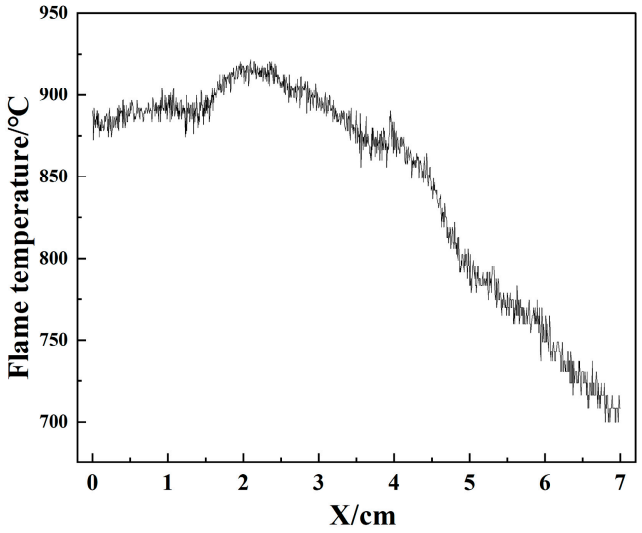


Figure 13. Centerline temperature change curve of nitrocellulose flame at 1000 ms.

Figure 14 is the maximum temperature change curve of nitrocellulose flame within 0–2000 ms. The "TC temperature" in Figure 14 is the flame temperature measured by our two-color method, which is more in line with the characteristics of energetic material combustion, due to the sudden release of energy contained in the ignition moment. It will reach a higher temperature at the beginning; the temperature of nitrocellulose flame at the start reaches 978.4 °C. The fuel begins to diffuse outward, the temperature drops significantly, and the temperature rises slightly. The stable combustion is about 925 °C. After 750 ms, the flame obtains a large amount of oxygen, and the internal alkali metal combustion releases more heat, causing the flame to reach the maximum temperature of 993.7 °C. After 1250 ms, the energetic material gradually decreases. The flame temperature also began to gradually decrease, dropping to 825.2 °C at 2000 ms.

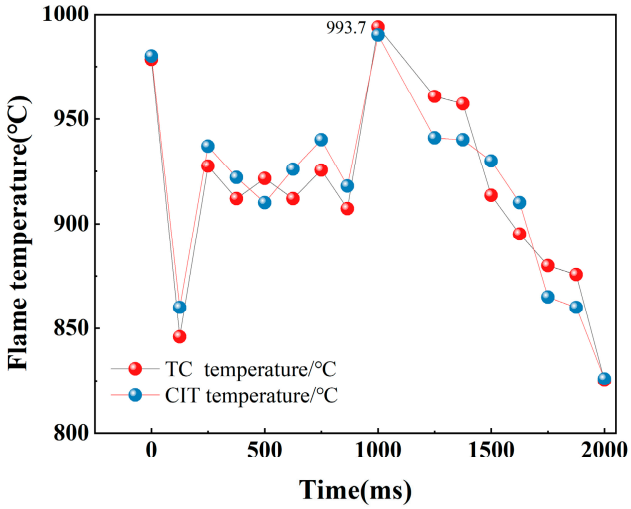


Figure 14. Temperature change curve of 0.3 g nitrocellulose flame.

We used the CIT-3MD2-T0830&T0409-W34-HS20us two-color infrared thermometer from CASSCIT company (Beijing, China) in China to collect the nitrocellulose flame temperature at the same time. It can only collect the maximum temperature of the effective area in the form of point temperature and cannot obtain the two-dimensional temperature distribution of the flame. The temperature measurement range is 400–3000 °C, the temperature measurement accuracy is 1% *Tm*, the response time is 20 us, and the collected temperature is named CIT temperature.

As can be seen from the image, compared with the mature two-color infrared thermometer, the temperature change trend of the flame is consistent, and the maximum relative temperature measurement error of 0.3 g nitrocellulose flame is 2.09%.

In addition, we performed 0.1 g and 0.2 g nitrocellulose flame temperature tests, and the maximum flame temperature measured by our two-color method was 804 °C and 862 °C, as shown in Figures 15 and 16.

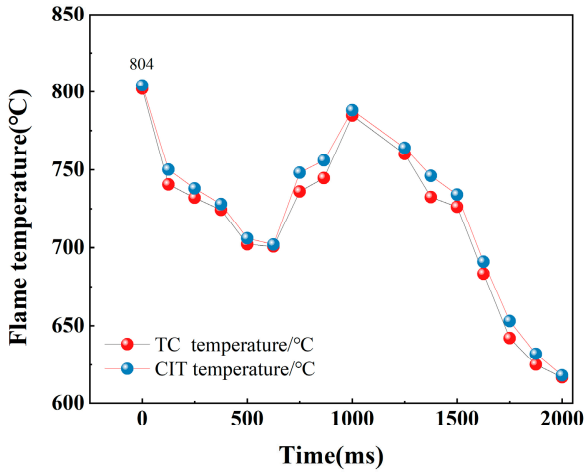


Figure 15. Temperature change curve of 0.1 g nitrocellulose flame.

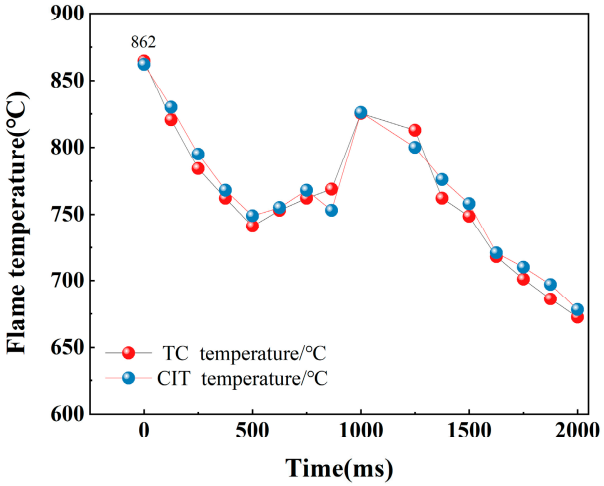


Figure 16. Temperature change curve of 0.2 g nitrocellulose flame.

The flame temperature change trend is also very consistent with that of the mature two-color infrared thermometer, where the maximum temperature occurs at the beginning time, and the maximum relative temperature measurement error is 1.82% and 2.10%.

In order to further verify the correctness of the temperature measurement technology in this paper, we compare it with the currently advanced TDLAS (Tunable Diode Laser Absorption Spectroscopy) technology [47] and analyze the temperature measurement accuracy of the highest temperature of 0.3 g, 0.2 g, 0.1 g nitrate flame data, both without noise and with 5% noise. The temperature measurement data are shown in Table 5:

Table 5. Comparison of TC and TDLAS.

	0.3 g		0.2 g		0.1 g	
	0%	5%	0%	5%	0%	5%
TC temperature (°C)	993.7	991.2	862	859.4	804	800.6
TDLAS temperature (°C)	1012.6	1012.6	878.2	878.2	818	818
Error (%)	1.87%	2.11%	1.84%	2.14%	1.71%	2.13%

From the above data comparison, it is found that compared with the two-color temperature measurement method, the relative error of temperature measurement is about 1.80%, and the error of adding 5% noise is about 2.2%, indicating that the method has good robustness in noise environment.

4. Discussion

In this study, the combustion radiation spectrum was obtained by LIBS technology, and the optimal temperature measurement line was selected according to the principle of two-color thermometry. Compared with the current randomly selected temperature measurement line, it has a higher temperature measurement accuracy. In addition, a temperature measurement system is constructed using a high-spatially resolved camera, which can measure the high spatial distribution of flame temperature. Since the temperature test distance of nitrocellulose flame is 50 cm, the effects of radiation reabsorption along the measurement path length are not considered in this study, and the above problems will be studied in depth when long-distance measurements are carried out in the future.

5. Conclusions

In summary, we report a high-resolution, low-cost, and quickly realized flame temperature detection scheme based on an sCMOS camera. LIBS (Laser-Induced Breakdown Spectroscopy) technology is used to hit the combustion product of nitrocellulose, obtain the characteristic spectral information of nitrocellulose, and select the optimal spectral line based on the principle of two-color temperature measurement to avoid the influence of emissivity on temperature measurement accuracy. The sCMOS camera was combined with 694 nm and 768 nm filters to build a temperature measurement system, and a temperature calibration experiment was conducted to detect and image the flame temperature of the energy-containing material nitrocellulose. The maximum temperature measurement error and temperature measurement uncertainty of this method are 2.10% and 3.43%. Compared to traditional two-color infrared thermometers, it provides a new idea for realizing higher resolution, low cost, and more accurate flame temperature 2D detection technology. In the future, this technology can be applied to the fields of explosion field temperature and industrial boiler temperature.

Author Contributions: Conceptualization, P.P. and X.H.; validation, X.H. and P.P.; formal analysis, S.F.; investigation, T.W., C.X. and P.P.; original draft preparation, P.P. and X.H.; review and editing, X.H. and C.X.; funding acquisition, X.H. All authors have read and agreed to the published version of the manuscript.

Funding: This research was funded by National Natural Science Foundation of China (52475575); National Natural Science Foundation of China (52075504); State Key Laboratory of Quantum Optics and Quantum Optics Devices (KF202301); Shanxi Provincial Key Research and Development Project (202302150101016); Central Guided Local Science and Technology Development Funding Program (YDZJSX2024D033).

Institutional Review Board Statement: Not applicable.

Informed Consent Statement: Not applicable.

Data Availability Statement: Data underlying the results presented in this paper are not publicly available at this time but may be obtained from the authors upon reasonable request.

Acknowledgments: The authors thank all the reviewers, editors, and contributors for their contributions and suggestions, as well as all the members of the OSEC Laboratory.

Conflicts of Interest: The authors declare no conflicts of interest.

References

1. Wang, Y.Q.; Chen, Y.R.; Zhao, Q.; Zhou, M.; Shao, Y. On-Line Measurement of Converter Combustion Flame with Radiation Thermometry and AES. *Spectrosc. Spect. Anal.* **2017**, *37*, 1243–1247. [CrossRef]
2. Li, S.Y.; Zhang, D.Y.; Gao, Q.; Li, B.; He, Y.; Wang, Z. Temperature measurement in a combustion flow field with femtosecond laser-induced filament. *Acta Phys. Sin.* **2020**, *69*, 234207. [CrossRef]
3. Olabode, O.F.; Fletcher, S.; Longstaff, A.P.; Bell, A. Core temperature measurement using ultrasound for high-precision manufacturing processes. *Proc. Inst. Mech. Eng. B J. Eng. Manuf.* **2023**, *237*, 09544054221150662. [CrossRef]
4. Zhang, B.Q.; Xu, Z.Y.; Liu, J.G.; Yao, L.; Ruan, J.; Hu, J.; Xia, H.; Nie, W.; Yuan, F.; Kan, R. Temperature measurement method of high temperature and high-pressure flow field based on wavelength modulation spectroscopy technology. *Acta Phys. Sin.* **2019**, *68*, 233301. [CrossRef]
5. Wang, Z.H.; Fu, P.F.; Hou, L.Y.; Chao, X. Diffuse-reflection-based single-ended laser absorption sensor for H2O temperature and concentration in kerosene-fuelled combustor. *Meas. Sci. Technol.* **2020**, *31*, 105202. [CrossRef]
6. Lee, D.N.; Cho, J.Y. Simplified stochastic temperature model for storage reliability estimation of solid rocket propellants. *J. Mech. Sci. Technol.* **2023**, *37*, 411–425. [CrossRef]
7. Kim, D.; Kubota, Y.; Izato, Y.; Miyake, A. Temperature variation measurements of an ignited energetic ionic liquid. *Sci. Technol. Energetic Mater.* **2023**, *84*, 14–16.

8. Tang, C.; Wang, Y.; Li, Y.; Zeng, S.; Kong, L.; Li, L.; Sun, J.; Zhu, M.; Deng, T. A review of graphene-based temperature sensors. *Microelectron. Eng.* **2023**, *275*, 112015. [CrossRef]
9. Hulewicz, A.; Dziarski, K.; Krawiecki, Z. The Estimated Temperature of the Semiconductor Diode Junction on the Basis of the Remote Thermographic Measurement. *Sensors* **2023**, *23*, 1944. [CrossRef]
10. Yu, Q.; Sun, X.; Gu, S.; Dong, Y. Study on CCD temperature measurement method without channel proportional coefficient calibration. *Opt. Laser Technol.* **2023**, *165*, 109625. [CrossRef]
11. Huang, J.; Li, S.; Sanned, D.; Xu, L.; Xu, S.; Wang, Q.; Stiti, M.; Qian, Y.; Cai, W.; Berrocal, E.; et al. A detailed study on the micro-explosion of burning iron particles in hot oxidizing environments. *Combust. Flame* **2022**, *238*, 111755. [CrossRef]
12. Hsu, P.S.; Jiang, N.; Felver, J.J.; Lauriola, D.K.; Danehy, P.M.; Roy, S. 10 kHz two-color OH PLIF thermometry using a single burst-mode OPO. *Opt. Lett.* **2021**, *46*, 2308–2311. [CrossRef]
13. Satija, A.; Lucht, R.P. Simultaneous Temperature and Pressure Measurements in Compressible Flow Using Nanosecond O2 Coherent Anti-Stokes Raman Spectroscopy. *Appl. Spectrosc.* **2022**, *76*, 541–547. [CrossRef] [PubMed]
14. Moller, S.; Käufer, T.; Pandey, A.; Schumacher, J.; Cierpka, C. Combined particle image velocimetry and thermometry of turbulent superstructures in thermal convection. *J. Fluid Mech.* **2022**, *945*, A22. [CrossRef]
15. Wang, L.Y.; Du, H.M.; Xu, H. Compensation method for infrared temperature measurement of explosive fireball. *Thermochim. Acta* **2019**, *680*, 178342. [CrossRef]
16. Li, Y.; Pan, D.; Jiang, Z.; Yu, H.; Gui, W. Adaptive Compensation Method for the Infrared Temperature Measurement Error Based on 3D Thermal Imaging. *IEEE Sens. J.* **2023**, *23*, 13200–13208.
17. Lin, J.; Zhang, X.; Liu, K.; Zhang, W. Emissivity characteristics of hydrocarbon flame and temperature measurement by color image Processing. *Energies* **2019**, *12*, 2185. [CrossRef]
18. Li, C.; Kong, D.; Wang, Y.; Gao, L.; Zhang, X.; Zhang, Q. Color CCD High-Temperature Measurement Method Based on Matrix Searching. *Appl. Sci.* **2023**, *13*, 5334. [CrossRef]
19. Zhang, X.; Zeng, C.B.; Liu, X.Y.; Chen, P.; Han, Y. Multispectral Temperature Measurement Method Based on Multivariate Extreme Value Optimization. *Spectrosc. Spect. Anal.* **2023**, *43*, 705–709.
20. Wang, Z.; Dai, J.; Yang, S. The development of a multispectral pyrometer for achievable proper temperature field measurements of the explosion flame. *Meas. Sci. Technol.* **2023**, *34*, 065501. [CrossRef]
21. Campbell, N.R.; Gardiner, H.W.B. Photo-electric colour-matching. *J. Sci. Instrum.* **1925**, *2*, 177–187.
22. Zhou, H.C.; Lou, C.; Cheng, Q. Experimental investigations on visualization of three-dimensional temperature distributions in a large-scale pulverized-coal-fired boiler furnace. *Proc. Combust. Inst.* **2005**, *30*, 1699–1706. [CrossRef]
23. Luo, Z.; Zhou, H.C. A combustion-monitoring system with 3-D temperature reconstruction based on flame-image processing technique. *IEEE Trans. Instrum. Meas.* **2007**, *56*, 1877–1882. [CrossRef]
24. Yan, W.; Zhou, H.; Jiang, Z.; Lou, C.; Zhang, X.; Chen, D. Experiments on measurement of temperature and emissivity of municipal solid waste (MSW) combustion by spectral analysis and image processing in visible spectrum. *Energy Fuels* **2013**, *27*, 6754–6762. [CrossRef]
25. Huang, Y.; Long, M.; Fan, H.; Gui, L.; Chen, D.; Duan, H. Quantifying the Effects of Combustion Gases' Radiation on Surface Temperature Measurements Using Two-Color Pyrometry. *Energy Fuels* **2019**, *33*, 3610–3619. [CrossRef]
26. Huang, Y.; Long, J.; Chen, D.; Long, M.; Yang, Z.; Li, C. Temperature errors in two-color pyrometry simultaneously considering reflection and combustion gas radiation. *Opt. Express* **2021**, *29*, 25084–25099. [CrossRef]
27. Zhang, Q.W.; Cheng, Y.F.; Xia, Y.; Wang, Z.; Wang, Q.; Shen, Z. Application of two-color thermometry pyrometer in the measurement of transient explosion temperature. *Explos. Shock Waves* **2022**, *42*, 114101.
28. Li, C.; Xu, C.; Wang, Y.; Gao, L.; Zhang, X.; Zhang, Q.; Kong, D. Study on the Influence of Internal Modulation Parameters on the Temperature Calculation Performance of Matrix-Searching CCD Pyrometer. *Meas. Sci. Technol.* **2024**, *35*, 36002. [CrossRef]
29. Cheng, Y.F.; Yao, Y.L.; Wang, Z.H.; Zhang, B.B.; Xia, Y.; Liu, R.; Shu, C.M. An improved two-colour pyrometer based method for measuring dynamic temperature mapping of hydrogen-air combustion. *Int. J. Hydrogen Energy* **2021**, *46*, 34463–34468. [CrossRef]
30. Corral-Gómez, L.; Armas, O.; Soriano, J.A.; Pastor, J.; Garcia-Oliver, J.M.; Mico, C. An Optical Engine Used as a Physical Model for Studies of the Combustion Process Applying a Two-Color Pyrometry Technique. *Energies* **2022**, *15*, 4717. [CrossRef]
31. Sawada, S.; Okada, D.; Nakatsuka, N.; Tainaka, K.; Hori, T.; Hayashi, J.; Akamatsu, F. Effects of ambient temperature on the combustion processes of single pulverized coal particle. *J. Therm. Sci. Technol.* **2021**, *16*, JTST0011. [CrossRef]
32. Hu, K.; Xu, Y.; Li, M.; Gu, X. Research on 2D Temperature Field Measurement Method of Mg/CO2 Combustion Flame Based on Color CCD. *IOP Conf. Ser. Earth Environ. Sci.* **2021**, *631*, 012116. [CrossRef]
33. Yu, T.; Bauer, F.J.; Huber, F.J.; Will, S.; Cai, W. 4D temperature measurements using tomographic two-color pyrometry. *Opt. Express* **2021**, *29*, 5304–5315. [CrossRef] [PubMed]
34. Xu, X.G.; Wei, K.P.; Feng, L.H.; Yang, B.; Ping, L.; Xu, Q.; Liu, J.; Wang, Y. Research on Radiation Spectroscopy Thermometry of Plume of Solid Rocket Motor. *Spectrosc. Spect. Anal.* **2021**, *41*, 305–311.

35. Hao, W.Y.; Hao, X.J.; Yang, Y.W.; Liu, X.; Liu, Y.; Sun, P.; Sun, R. Rapid classification of soils from different mining areas by laser-induced breakdown spectroscopy (LIBS) coupled with a PCA-based convolutional neural network. *J. Anal. At. Spectrom.* **2021**, *36*, 2509–2518. [CrossRef]
36. Jin, H.Y.; Hao, X.J.; Mo, B.M. Rapid classification of heavy metal soils from different mining areas by using a GSCV quadratic merit seeking network combined with MF-LIBS. *J. Anal. At. Spectrom.* **2023**, *38*, 2280–2290. [CrossRef]
37. Mason, P.E.; Darvell, L.I.; Jones, J.M.; Williams, A. Observations on releasing gas-phase potassium during the combustion of single biomass particles. *Fuel* **2016**, *182*, 110–117. [CrossRef]
38. De Lucia, F.C.; Harmon, R.S.; McNesby, K.L.; Winkel, R.J.J.; Miziolek, A.W. Laser-induced breakdown spectroscopy analysis of energetic materials. *Appl. Opt.* **2003**, *42*, 6148–6152. [CrossRef]
39. Kramida, A.; Ralchenko, Y.; Reader, J.; NIST ASD Team. NIST Atomic Spectra Database (Version 5.10). Available online: https://physics.nist.gov/asd (accessed on 24 September 2024).
40. Liu, X.D.; Hao, X.J.; Xue, B.; Tai, B.; Zhou, H. Two-dimensional flame temperature and emissivity distribution measurement based on element doping and energy spectrum analysis. *IEEE Access* **2020**, *8*, 200863–200874. [CrossRef]
41. Sun, Y.; Lou, C.; Zhou, H. A simple judgment method of gray property of flames based on spectral analysis and the two-color method for measurements of temperatures and emissivity. *Proc. Combust. Inst.* **2011**, *33*, 735–741. [CrossRef]
42. Xue, B.; Hao, X.J.; Liu, X.D.; Tai, B.; Zhou, H. Simulation of an NSGA-III based fireball inner-temperature-field reconstructive method. *IEEE Access* **2020**, *8*, 43908–43919.
43. Wang, J.; Hao, X.J.; Pan, B.W.; Huang, X.; Sun, H.; Pei, P. Spectroscopic measurement of the two-dimensional flame temperature based on a perovskite single photodetector. *Opt. Express* **2023**, *31*, 8098–8109. [CrossRef] [PubMed]
44. Wang, J.; Hao, X.J.; Pan, B.W.; Huang, X.; Sun, H.; Pei, P. Perovskite single-detector visible-light spectrometer. *Opt. Lett.* **2023**, *48*, 399–402. [CrossRef] [PubMed]
45. Tucsen Photonics Co., Ltd. Dhyana 400BSI V2. Available online: https://www.tucsen.com/Home/Product/info/dataid/27.html (accessed on 2 September 2024).
46. Monier, R.; Thumerel, F.; Chapuis, J.; Soulie, F.; Bordreuil, C. Liquid metals surface temperature fields measurements with a two-colour pyrometer. *Measurement* **2017**, *101*, 72–80. [CrossRef]
47. Huang, X.; Hao, X.; Pan, B.; Liang, X.; Wang, Z.; Feng, S.; Pei, P.; Zhang, H. Flame Imaging Technology Based on 64-Pixel Area Array Sensor. *Micromachines* **2024**, *15*, 44. [CrossRef]

Disclaimer/Publisher's Note: The statements, opinions and data contained in all publications are solely those of the individual author(s) and contributor(s) and not of MDPI and/or the editor(s). MDPI and/or the editor(s) disclaim responsibility for any injury to people or property resulting from any ideas, methods, instructions or products referred to in the content.